# Dependence of thermodynamic quantities at freeze-out on pseudorapidity and collision energy in *p-p* collisions at LHC energies*

Murad Badshah[1†] Yahia A.H. Obaidat[2] Haifa I. Alrebdi[3‡] M. Waqas[4§] Muhammad Ajaz[1¶] Refka Ghodhbani[5]

[1]Department of Physics, Abdul Wali Khan University Mardan, Mardan 23200, Pakistan
[2]Department of Physics, College of Science, University of Bisha, Bisha 61922, Saudi Arabia
[3]Department of Physics, College of Science, Princess Nourah bint Abdulrahman University, Riyadh 11671, Saudi Arabia
[4]School of Mathematics, Physics and Optoelectronic Engineering, Hubei University of Automotive Technology, Shiyan 442002, China
[5]Department of Computer Sciences, Faculty of Computing and Information Technology, Northern Border University, Rafha, Saudi Arabia

**Abstract:** The transverse momentum distributions of charged hadrons produced in proton-proton collisions at center-of-mass energies ( $\sqrt{s}$) of 0.9 TeV and 2.36 TeV, as measured by the CMS detector at the Large Hadron Collider (LHC), have been analyzed within various pseudorapidity classes utilizing the thermodynamically consistent Tsallis distribution. The fitting procedure resulted in the key parameters, namely, effective temperature ($T$), non-extensivity parameter ($q$), and kinetic freezeout volume ($V$). Additionally, the mean transverse momentum ($\langle p_T \rangle$) and initial temperature ($T_i$) of the particle source are determined through the fit function and string percolation method, respectively. An alternative method is employed to calculate the kinetic freezeout temperature ($T_0$) and transverse flow velocity ($\beta_T$) from $T$. Furthermore, thermodynamic quantities at the freezeout, including energy density ($\varepsilon$), particle density ($n$), entropy density ($s$), pressure ($P$), and squared speed of sound ($C_s^2$), are computed using the extracted $T$ and $q$. It is also observed that, with a decrease in pseudorapidity, all thermodynamic quantities except $V$ and $q$ increase. This trend is attributed to greater energy transfer along the mid pseudorapidity. $q$ increases towards higher values of pseudorapidity, indicating that particles close to the beam axis are far from equilibrium. Meanwhile, $V$ remains nearly independent of pseudorapidity. The excitation function of these parameters ($q$) shows a direct (inverse) correlation with collision energy. The $\varepsilon$, $n$, $s$, and $P$ show a strong dependence on collision energies at low pseudorapidities. Explicit verification of the thermodynamic inequality $\varepsilon \geqslant 3P$ suggests the formation of a highly dense droplet-like Quark-Gluon Plasma (QGP). Additionally, the inequality $T_i > T > T_0$ is explicitly confirmed, aligning with the evolution of the produced fireball.

**Keywords:** charged hadrons, tsallis statistics, effective temperature, non-extensivity parameter, pseudorapidity, kinetic freeze-out stage, multiple freeze-out scenario, QGP, QCD matter, squared speed of sound

**DOI:** 10.1088/1674-1137/ad62da

## I. INTRODUCTION

The concepts of confinement and asymptotic freedom within Quantum Chromodynamics (QCD) have sparked numerous discussions regarding the thermal and transport characteristics of highly dense and hot matter. According to confinement principles, nuclear matter is assumed to consist of low-energy hadrons, forming a sparsely interacting gas of these particles. Conversely, at ultra-relativistic energies, asymptotic freedom implies extremely weak interactions between quarks and gluons, depicting nuclear matter as a weakly interacting gas of these constituents. It is believed that a phase transition occurs between these configurations, leading to the disappearance of hadrons' degrees of freedom and the formation of Quark–Gluon Plasma (QGP), achievable at very high temperatures or densities [1−6]. QGP was present during the early universe, a few microseconds post-Big Bang, and potentially exists in certain forms within the cores of neutron stars. The occurrence of ultra-relativistic heavy-

Received 9 May 2024; Accepted 13 July 2024; Published online 14 July 2024

* Supported by Princess Nourah bint Abdulrahman University Researchers Supporting Project number (PNURSP2024R106), Princess Nourah bint Abdulrahman University, Riyadh, Saudi Arabia. In addition, the authors extend their appreciation to the Deanship of Scientific Research at Northern Border University, Arar, KSA for funding this research work through the project number "NBU-FFR-2024-2461-04"

† E-mail: murad_phy@awkum.edu.pk
‡ E-mail: hialrebdi@pnu.edu.sa
§ E-mail: 20220073@huat.edu.cn
¶ E-mail: ajaz@awkum.edu.pk

ion collisions has provided a systematic means to generate and explore various phases of bulk nuclear matter.

Multiple experiments conducted at facilities like the Super Proton Synchrotron (SPS) [7, 8], Relativistic Heavy Ion Collider (RHIC) [9, 10], and Large Hadron Collider (LHC) [11, 12] have yielded extensive experimental data. The experiments conducted on the nucleus-nucleus ($A$-$A$) collisions at RHIC and LHC have led particle and nuclear physicists to announce the discovery of QGP in 2000 [13, 14]. Proton–proton ($p$-$p$) collisions are fundamental for establishing a base to explore collisions involving heavy ions ($A$-$A$) or proton-nucleus (pA). In the $A$-$A$ collisions, collective flow emerges as a notable feature within the dense thermal medium of this strongly interactive substance (QGP) [15, 16]. High-multiplicity $p$-$p$ collision events have also exhibited this collective behaviour [17, 18]. Other notable features observed in high-multiplicity $p$-$p$ events include increased strangeness [19]; the generation of a substantial number of particles [20]; equivalent values of effective temperature, kinetic freeze-out temperature, and flow velocity compared to those seen in $A$-$A$ collisions [21, 22]; and correlations akin to multi-particle ridges [23]. Therefore, it is crucial to conduct thorough investigations into $p$-$p$ collisions.

To obtain the freeze-out parameters, different methods, models, and techniques are used, and their extraction from the $p_T$ of charged particles is one of the most common methods. $p_T$ distributions carry true information about the kinetic freeze-out stage of the expanding system because at and after this stage, the particles do not exchange their energies and momenta till their arrival at the detectors. Different statistical and hydrodynamical models are incorporated to extract or decode the information from the $p_T$ spectra. The heavy ion collision results in the production of an intricate system in which particles are not in the thermal equilibrium and have long-range correlations. Under such conditions, models like the Boltzmann-Gibbs distribution function [24] and Blast Wave model [25] cannot explain this system precisely as they consider the produced system to be in thermal equilibrium; the Tsallis model is best suited for such an intricate non-equilibrated system with its non-extensive parameter ($q$). Moreover, the Tsallis distribution exhibits a power-law tail allowing for a good fit to high $p_T$ regions, while the other models may behave inadequately in high $p_T$ regions. Based on thermodynamic consistency, the Tsallis distribution may either be thermodynamically consistent or inconsistent [26-28]; the earlier consistently obeys all the basic thermodynamic laws while the latter does not. Due to the aforementioned preferences of the Tsallis distribution over the others and keeping the thermodynamic consistency in view, we use the thermodynamically consistent Tsallis model in the present analysis to describe the $p_T$ distribution of charged hadrons in $p$-$p$ collision at $\sqrt{s}$ = 0.9 TeV and 2.36 TeV in different pseudorapidity ($\eta$) intervals.

There are two ways to extract the parameters: directly and indirectly. Extracting the effective temperature, non-extensive parameter, and kinetic freeze-out volume of the system from the fitting of the thermodynamically consistent Tsallis model with the $p_T$ distribution is the direct way of extracting parameters, while $T_0$ and $\beta_T$ are extracted indirectly. Additionally, other very crucial thermodynamic quantities, including $T_i$, energy density ($\varepsilon$), particle density ($n$), entropy density ($s$), pressure ($P$), and squared speed of sound ($C_s^2$), are also calculated at different values of $\eta$ at $\sqrt{s}$ = 0.9 TeV and 2.36 TeV. All of these parameters are very significant to the equation of state of the system, as they all define different physical states of the system at distinct stages of the evolution of the system, from the initial stages to the stage of thermal freeze-out. In the present analysis, the average values of $\eta$ intervals have been used. For instance, for the $\eta$ interval of 0−0.2, 0.1 has been used; similarly for the interval 0.2−0.4, 0.3 has been used, etc.

In our prior studies [29, 30] and [31, 32], we examined the changing tendencies of the freeze-out parameters concerning alterations in collision energies and centrality, respectively. The current study focuses on the scrutiny of the parameters $T$, $q$, $V$, $T_0$, $\beta_T$, $T_i$, $\varepsilon$, $n$, $s$, $p$, and $C_s^2$, particularly their reliance on $\eta$ and collision energies.

The remainder of this paper is structured as follows: Section II outlines the model applied in this study. Following that, the Section III details the outcomes, and Section IV gives the conclusions of this research endeavour.

## II. METHOD AND FORMALISM

The standard thermal models like standard distribution and Boltzmann-Gibbs distribution consider the particles of the produced system in thermal equilibrium. However, the system produced in high-energy collisions is away from thermal equilibrium. The Tsalis distribution, with its non-extensive parameter, is the better choice to study such a system as it does not consider the system in thermal equilibrium. There are various forms of the Tsallis distribution function, among which we have used the one best suited to the currently analyzed experimental data. This form of the Tsallis distribution function is given by [33]

$$\frac{\mathrm{d}^2N}{\mathrm{d}p_T\,\mathrm{d}y} = gV\frac{p_T\,m_T\,\cosh(y)}{(2\pi)^2} \times\left[1+(q-1)\frac{m_T\,\cosh(y)-\mu}{T}\right]^{\frac{q}{(1-q)}}. \quad (1)$$

Where $g$ is the degeneracy factor, and $V$, $T$, and $\mu$ are the volume of the produced system, effective temperature and chemical potential, respectively. $q$ is the non-extens-

ivity parameter, which measures how far or close a system is to the thermal equilibrium. Generally, $q > 1$ represents a system away from the thermal equilibration. For $q = 1$, the Tsallis distribution simplifies to the Boltzmann-Gibbs distribution, which considers the system to be in thermal equilibrium. $m_T$ is the transverse mass given by $m_T = \sqrt{p_T^2 + m_0^2}$, where $m_0$ is the rest mass of the produced charged hadron [34]. The effective temperature is a temperature-like parameter that includes both the thermal effect, in the form of kinetic freeze-out temperature ($T_0$), and the flow effect, in the form of transverse flow velocity ($\beta_T$), of the QGP medium and is defined as [35, 36] $T = T_0 + m_0\beta_T$.

At RHIC and LHC, due to the symmetric production of particles and anti-particles, the chemical potential is assumed to be zero. Now, at $\mu = 0$ and at mid rapidity $y = 0$. Eq. (1) can be written as

$$\frac{\mathrm{d}^2N}{\mathrm{d}p_T\,\mathrm{d}y} = gV\frac{p_T\,m_T}{(2\pi)^2}\left[1+(q-1)\frac{m_T}{T}\right]^{\frac{q}{(1-q)}}. \tag{2}$$

In high-energy collisions, $\eta$ is often used instead of $y$, where the conversion between the two is given as

$$\frac{\mathrm{d}y}{\mathrm{d}\eta} = \sqrt{1-\frac{{m_0}^2}{m_T^2\cosh^2 y}}. \tag{3}$$

Using Eq. (3) in Eq. (2), the pseudorapidity distribution at $y = 0$ is given in the following form [37]:

$$\frac{\mathrm{d}^2N}{\mathrm{d}p_T\,\mathrm{d}\eta} = gV\frac{{p_T}^2}{(2\pi)^2}\left[1+(q-1)\frac{m_T}{T}\right]^{\frac{q}{(1-q)}}. \tag{4}$$

The above Tsallis distributions are individual particle distributions as they satisfy the experimental $p_T$ spectra for only a single particle at a time. As charged particles are dealt with in this work, which contains $\pi^{\pm}$, $K^{\pm}$ and $p(\bar{p})$, there should be three Tsallis distributions each for the separate species of particles. Under such conditions, Eq. (4) is written as

$$\frac{\mathrm{d}^2N}{\mathrm{d}p_T\,\mathrm{d}\eta} = 2\sum_{i=1}^{3} g_i V\frac{{p_T}^2}{(2\pi)^2}\left[1+(q-1)\frac{m_{T,i}}{T}\right]^{\frac{q}{(1-q)}}. \tag{5}$$

Here, $i = \pi^+, K^+$, and $p$, while $m_{T,i}$ is the mass of particle $i$. The factor of 2 is introduced in the above equation to account for the equal contributions from the anti-particles because both particles and their antiparticles are estimated to be equally produced at high energies in RHIC and LHC.

It is important to note that one could argue that Eq. (5) is inappropriate for the two types of particles with roughly equal masses, the proton and phi meson ($\phi$); as their degeneracy factors are 2 and 3, respectively, their yield ratio is 2/3 in accordance with Eq. (5), which may be different from the experimentally measured yield ratio. The distribution can be a helpful tool for fitting the transverse momentum spectra of particles generated in collisions with high energies. It works well for capturing the power law behaviour and non-thermal features found in the momentum spectra of different particles, not just pions. Nevertheless, when degeneracy factors and observed yield ratios diverge significantly, the model is not fully capable of predicting yield ratios for various species of particles. Proton-to-phi meson yield ratio, as measured by ALICE and other experimental groups, differs from that estimated by the Tsallis distribution-based degeneracy factors. Despite the Tsallis distribution's good fit to the $p_T$ spectra, this discrepancy suggests that it does not naturally take into consideration the complexity of particle yields. When predicting particle yields, the Tsallis distribution is not very accurate. It excludes elements that are critical for precise yield estimates and have a substantial impact on the relative abundances of various particle species, such as resonance decays and other post-collision interactions. Consequently, when employing the fitting of $p_T$ spectra of charged particles such as protons, kaons, and phi mesons, Eq. (5) is accurate.

Regardless of the form of particle momentum distribution, the $p_T$-dependent probability density function is given as follows [38]:

$$f(p_T) = \frac{1}{N}\frac{\mathrm{d}N}{\mathrm{d}p_T}. \tag{6}$$

Which is naturally normalized to unity.

$$\int_0^{\infty} f(p_T)\,\mathrm{d}p_T = 1. \tag{7}$$

The mean transverse momentum, $\langle p_T\rangle$, can be obtained directly from the fit function by using the probability density function in the following form:

$$\langle p_T\rangle = \frac{\int_0^{\infty} p_T\,f(p_T)\,\mathrm{d}p_T}{\int_0^{\infty} f(p_T)\,\mathrm{d}p_T}. \tag{8}$$

Making use of Eq. (7), we get,

$$\langle p_T\rangle = \int_0^{\infty} p_T\,f(p_T)\,\mathrm{d}p_T. \tag{9}$$

Similarly, the root mean square $p_T$ is given as

$$\sqrt{\langle {p_T}^2\rangle} = \sqrt{\frac{\int_0^\infty {p_T}^2\, f(p_T)\, \mathrm{d}p_T}{\int_0^\infty f(p_T)\, \mathrm{d}p_T}}. \tag{10}$$

$$\sqrt{\langle {p_T}^2\rangle} = \sqrt{\int_0^\infty {p_T}^2\, f(p_T)\, \mathrm{d}p_T}. \tag{11}$$

According to the string Percolation model [39–41], the initial temperature, $T_i$, of the system at the parton level is calculated by the following equation from $\sqrt{\langle {p_T}^2\rangle}$ ($p_{T\,rms}$):

$$T_i = \frac{p_{T\,rms}}{\sqrt{2}}. \tag{12}$$

The effective temperature is not a real temperature as it contains the thermal and flow effects, to obtain the real temperature at the kinetic freeze-out stage, called the kinetic freeze-out temperature ($T_0$), and the transverse flow velocity ($\beta_T$), the following two empirical formulae are used, respectively [42]:

$$T_0 = \frac{k_0\,\langle p_T\rangle}{2}, \tag{13}$$

$$\beta_T = \frac{(1-k_0)\,\langle p_T\rangle}{2\,m_0\,\bar{\gamma}}. \tag{14}$$

In high-energy *A-A* or *p-p* collisions, the participants from both projectile and target contribute equally to the $\langle p_T\rangle$. Therefore, according to the multi-source thermal model, each participant of projectile and target contributes 1/2 to $\langle p_T\rangle$ and each of these halves is equally contributed by the thermal and flow effects, which is why we introduced 2 in the denominator of Eq. (13) and Eq. (14). In the last two equations, $k_0$ and $1-k_0$ are the contribution fractions of thermal motion (thermal effects) and flow effects, respecitevly. The value of $k_0$ is collision energy dependent and is given as

$$k_0 = 0.03 - 0.01\ln(\sqrt{s}). \tag{15}$$

Where $\sqrt{s}$ is in the units of GeV. $\bar{\gamma}$ is the mean Lorentz factor and is given as follows:

$$\bar{\gamma} = \frac{\bar{E}}{m_0} \tag{16}$$

Because

$$\gamma = \frac{E}{m_0}. \tag{17}$$

Here, $E$ and $\bar{E}$ are energy and mean energy of the produced charged hadron, respectively. The energy in the source rest frame is formulated as follows for $c = 1$:

$$E = \sqrt{p^2 + {m_0}^2}, \tag{18}$$

Making use of $p_T = p\sin\theta$ or equivalently $p_T = p/\csc\theta$ in the above equation, we get,

$$E = \sqrt{(p_T\csc\theta)^2 + {m_0}^2}, \tag{19}$$

Where $\theta$ is the emission angle of the produced charged hadrons, which satisfies the following equation [42]:

$$\theta = 2\sin^{-1}(\sqrt{r}), \tag{20}$$

Here, $r$ is a number in the random loop [0,1] calculated through Monti-Carlo (MC) simulations. After repetitive calculations via the MC method, one can get $\bar{E}$ (also equal to the mean moving mass, $\bar{m}$). Now, using Eq. (20) in Eq. (19), one can get

$$\bar{E} = \sqrt{\left(p_T\csc\left(2\sin^{-1}(\sqrt{r})\right)\right)^2 + {m_0}^2}. \tag{21}$$

Incorporating this equation together with Eq. (16) in Eq. (14), one can obtain $\beta_T$. In the current analysis, we extract $T$, $V$, and $q$ with the help of Eq. (5) and then use $T$ and $q$ to calculate other thermodynamic quantities at freezeout. These thermodynamic quantities include $\varepsilon$, $n$, $s$, $P$, heat capacity at constant volume, and ${C_s}^2$, whose mathematical equations are given bellow [37]:

$$\varepsilon = 2\sum_{i=1}^{3} g_i \int \frac{\mathrm{d}^3p}{(2\pi)^3} E_i \left[1 + (q-1)\frac{E_i}{T}\right]^{\frac{q}{1-q}}, \tag{22}$$

$$n = 2\sum_{i=1}^{3} g_i \int \frac{\mathrm{d}^3p}{(2\pi)^3} \left[1 + (q-1)\frac{E_i}{T}\right]^{\frac{q}{1-q}}, \tag{23}$$

$$s = 2\sum_{i=1}^{3} g_i \int \frac{\mathrm{d}^3p}{(2\pi)^3} \left[\frac{E_i}{T}\left(1 + (q-1)\frac{E_i}{T}\right)^{\frac{q}{1-q}} + \left(1 + (q-1)\frac{E_i}{T}\right)^{\frac{1}{1-q}}\right], \tag{24}$$

$$P = 2\sum_{i=1}^{3} g_i \int \frac{\mathrm{d}^3 p}{(2\pi)^3} \frac{p^2}{3E_i} \left[1 + (q-1)\frac{E_i}{T}\right]^{\frac{q}{1-q}}, \tag{25}$$

$$C_{\mathrm{V}} = 2\sum_{i=1}^{3} g_i \frac{q}{T^2} \int \frac{\mathrm{d}^3 p}{(2\pi)^3} E_i^{\,2} \left[1 + (q-1)\frac{E_i}{T}\right]^{\frac{2q-1}{1-q}}, \tag{26}$$

$$C_{\mathrm{s}}^2(T) = \left(\frac{\partial P}{\partial \varepsilon}\right)_{\mathrm{V}} = \frac{s}{C_{\mathrm{V}}}. \tag{27}$$

In these equations, $E$ is the energy of the produced particles at the freeze-out stage.

## III. RESULTS AND DISCUSSION

In this analysis, we used the minimum $\chi^2$ method [43], which is

$$\chi^2 = \sum_i \frac{(R_i^{\mathrm{Exp}} - R_i^{\mathrm{Theor}})^2}{\sigma^2}, \tag{28}$$

where $R_i^{\mathrm{Exp}}$ denotes the experimental data, $\sigma$ is the associated measurement uncertainty, and $R_i^{\mathrm{Theor}}$ signifies the values computed using the function (model).

Figure 1 displays the double differential $p_T$ distribution of charged hadrons in $p$-$p$ collision at (a) $\sqrt{s}$ = 0.9 TeV and (b) $\sqrt{s}$ = 2.36 TeV at different values of pseudorapidity ($\eta$) measured by CMS at LHC [44]. Different geometrical symbols are incorporated to represent the experimental data for the $p_T$ distribution at different $\eta$, while the solid lines are the fit results obtained through the Tsallis distribution. Each plot of Fig. 1 has a Data/Fit ratio at its bottom, which shows the fit quality. It is obvious from the plots that the model is in good agreement with experimental data. The data points and corresponding fit lines for different $\eta$ are scaled with different factors to avoid the overlapping of the spectra over each other and to enhance their visibility. These scaling factors along with the other extracted parameters and $\chi^2/NDF$ are listed in Table 1.

In the present analysis, we discuss the correlation of freezeout and different thermodynamic properties with $\eta$ and collision energy; therefore, it is significant to quantify how strongly or weakly these parameters (quantities) are correlated with $\eta$ and collision energy. This can be done by using the Pearson Correlation Coefficient, defined as [45]

$$r_{xy} = \frac{\sum_{i=1}^{n}(x_i - \langle x\rangle)(y_i - \langle y\rangle)}{\sqrt{\sum_{i=1}^{n}(x_i - \langle x\rangle)^2 \sum_{i=1}^{n}(y_i - \langle y\rangle)^2}}, \tag{29}$$

where $x$ and $y$ are the two sets of parameters, and $\langle x\rangle$ and $\langle y\rangle$ are their mean values given by $\sum_{i=1}^{n} x_i/n$ and $\sum_{i=1}^{n} y_i/n$, respectively. Here, $n$ is the number of parameters in each set of data. The values of $r_{xy}$ range between ±1, with +1 being used for strong positive correlation and −1 for strong negative correlation. $r_{xy}$ = 0 means there is no correlation between the two sets of parameters.

For the estimation of uncertainty in $r_{xy}$, the following formula is used, where the data points are assumed to be

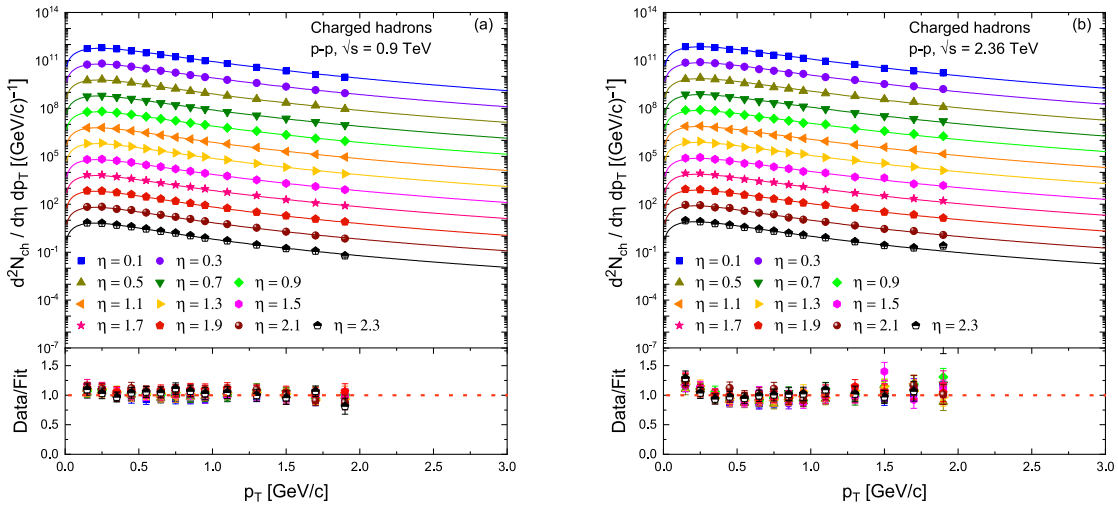


**Fig. 1.** (color online) Plots (a) and (b) display the double-differential $p_T$ spectra of charged hadrons for different values of $\eta$ at $\sqrt{s}$ = 0.9 TeV and 2.36 TeV, respectively [44]. Distinct colours and geometrical symbols indicate varying values of $\eta$. Solid lines represent the fitting results based on the Tsallis function. A Data/Fit ratio panel is included at the bottom of each plot to assess the fit quality.

**Table 1.** Values of different parameters extracted from the Tsallis distribution function, along with the values of $\chi^2$/NDF, where NDF is the number of degrees of freedom. The errors in a certain extracted parameter across different values of $\eta$ are very close to one another. Therefore, when these errors are rounded off to the third decimal place, they become almost the same, and such rounded-off errors are depicted in this table.

| collision | $\eta$ | Scaling factor | $T$ /GeV | $q$ | $V$ /fm$^3$ | $\chi^2$/NDF |
|---|---|---|---|---|---|---|
| *p-p* 0.9 TeV Fig. 1(a) | 0.1 | $10^{11}$ | 0.094±0.002 | 1.138±0.003 | 333±4.828 | 5.733/11 |
| | 0.3 | $10^{10}$ | 0.092±0.002 | 1.142±0.003 | 333±4.828 | 6.827/11 |
| | 0.5 | $10^{9}$ | 0.089±0.002 | 1.146±0.003 | 333±4.828 | 9.632/11 |
| | 0.7 | $10^{8}$ | 0.088±0.002 | 1.148±0.003 | 333±4.828 | 5.237/11 |
| | 0.9 | $10^{7}$ | 0.086±0.002 | 1.15±0.003 | 333±4.828 | 9.434/11 |
| | 1.1 | $10^{6}$ | 0.084±0.002 | 1.151±0.003 | 333±4.828 | 6.482/11 |
| | 1.3 | $10^{5}$ | 0.083±0.002 | 1.152±0.003 | 333±4.828 | 13.547/11 |
| | 1.5 | $10^{4}$ | 0.082±0.002 | 1.153±0.003 | 333±4.828 | 12.167/11 |
| | 1.7 | $10^{3}$ | 0.081±0.002 | 1.154±0.003 | 333±4.828 | 15.6437/11 |
| | 1.9 | $10^{2}$ | 0.079±0.002 | 1.155±0.003 | 333±4.828 | 21.641/11 |
| | 2.1 | 10 | 0.078±0.002 | 1.156±0.003 | 333±4.828 | 19.269/11 |
| | 2.3 | 1 | 0.075±0.002 | 1.157±0.003 | 333±4.828 | 13.379/11 |
| *p-p* 2.36 TeV Fig. 1(b) | 0.1 | $10^{11}$ | 0.104±0.003 | 1.132±0.003 | 442±6.409 | 11.334/11 |
| | 0.3 | $10^{10}$ | 0.103±0.003 | 1.133±0.003 | 442±6.409 | 13.036/11 |
| | 0.5 | $10^{9}$ | 0.102±0.003 | 1.134±0.003 | 442±6.409 | 13.309/11 |
| | 0.7 | $10^{8}$ | 0.101±0.003 | 1.136±0.003 | 442±6.409 | 11.276/11 |
| | 0.9 | $10^{7}$ | 0.097±0.003 | 1.142±0.003 | 442±6.409 | 19.6732/11 |
| | 1.1 | $10^{6}$ | 0.096±0.002 | 1.143±0.003 | 442±6.409 | 11.718/11 |
| | 1.3 | $10^{5}$ | 0.094±0.002 | 1.145±0.003 | 442±6.409 | 12.969/11 |
| | 1.5 | $10^{4}$ | 0.093±0.002 | 1.147±0.003 | 442±6.409 | 18.362/11 |
| | 1.7 | $10^{3}$ | 0.091±0.002 | 1.149±0.003 | 442±6.409 | 13.956/11 |
| | 1.9 | $10^{2}$ | 0.089±0.002 | 1.152±0.003 | 442±6.409 | 12.766/11 |
| | 2.1 | 10 | 0.084±0.002 | 1.153±0.003 | 442±6.409 | 14.203/11 |
| | 2.3 | 1 | 0.083±0.002 | 1.154±0.003 | 442±6.409 | 16.747/11 |

normally distributed with no linear correlation between the two sets of data points, *i.e.*, the null hypothesis is applied; the values of $S_r$ enable us to quantify how well the Pearson correlation fits normally or randomly distributed data:

$$S_r = \sqrt{\frac{1-r_{xy}^2}{n-2}}. \tag{30}$$

When the fireball is created, to achieve thermal equilibrium with its surroundings, it expands and cools down; during expansion and cooling there are two primary freeze-out stages. The stage at which inelastic collision between particles of the system vanishes, elastic interactions start, and the ratio of the particles turns to be fixed is called the chemical freeze-out stage, and the corresponding temperature of the system is called chemical freeze-out temperature. After the chemical freeze-out stage, the stage of thermal or kinetic freeze-out arrives, where the corresponding temperature is called thermal or kinetic freeze-out temperature, or even the effective temperature can also describe the kinetic freeze-out stage. At this stage, the mean free path of these particles becomes greater than the size of the system, and they get separated from the parent system and move towards the detectors. It must be noted that the thermodynamic quantities of the produced system have been calculated at the thermal and kinetic freeze-out stage.

In the following, the dependence of the freezeout parameters $T$, $q$, and $V$ and other thermodynamic quantities such as $\varepsilon$, $n$, $s$, $P$, and $C_s^2$ at the freeze-out will be discussed as a function of $\eta$ and collision energy.

### A. Effective temperature

Figure 2(a) displays the variation of $T$ as a function of $\eta$. Here the solid spheres represent various $T$ values at dif-

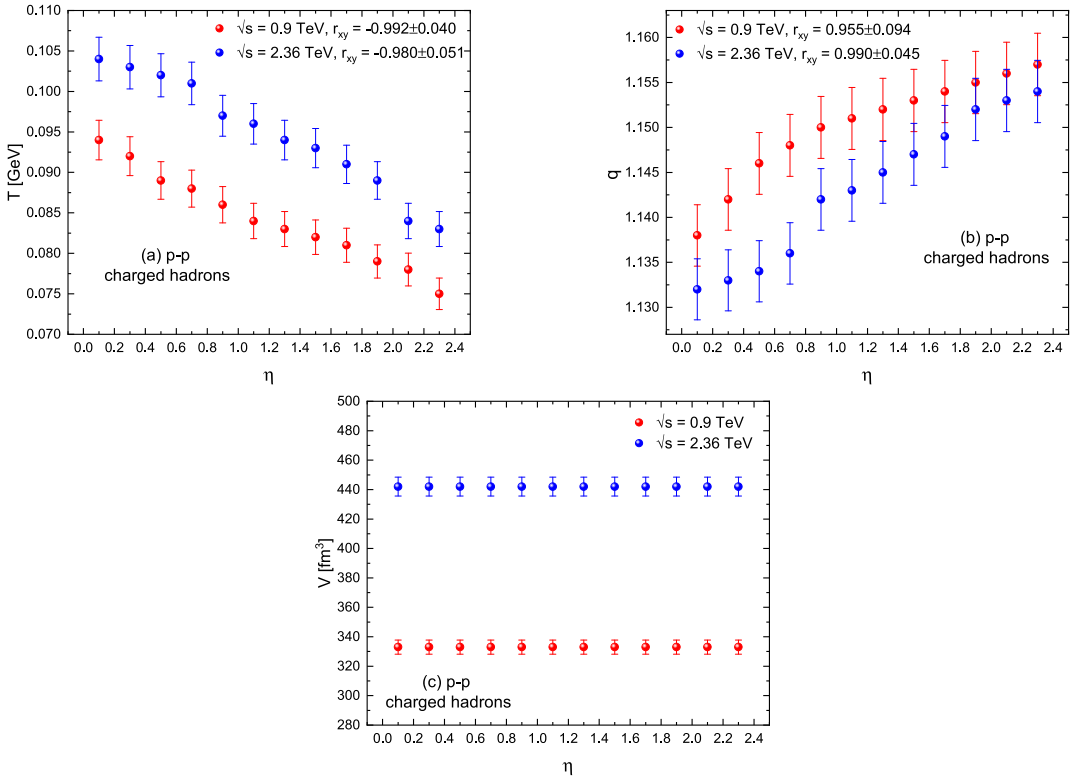


**Fig. 2.** (color online) (a) $T$, (b) $q$, and (c) $V$ extracted though the fitting procedure using the Tsallis function for charged hadrons, as a function of $\eta$ in $p$-$p$ collisions at $\sqrt{s}$ = 0.9 TeV and 2.36 TeV. The Pearson correlation coefficients along with their errors are displayed in the plots.

ferent $\eta$ intervals, and the two distinct colours indicate the two distinct collision energies. This figure suggests an inverse dependence of $T$ on $\eta$. The reason for this dependence is that the energy transfer to the system is greater along the mid $\eta$, which results in the higher excitation of the produced system. This energy transfer reduces as one moves towards the beam axis (higher values of $\eta$), either in the forward or backward direction, because of the greater penetration of the particles along the beam direction where some of its energy is lost while interacting with other particles. Here, by other particles, we mean the remnants of the colliding beams, the system produced close to the beam direction interacts with the beams' remnants, due to which, the system or produced particles lose some of their energy, which results in the low temperature along the beam direction (high $\eta$). The values of $r_{xy} = -0.992 \pm 0.040$ and $r_{xy} = -0.98 \pm 0.051$ for $\sqrt{s}$ = 0.9 and 2.36 TeV, respectively, suggest a strong negative relationship between $T$ and $\eta$. This figure also indicates that with increasing $\sqrt{s}$, $T$ increases because of the greater excitation of the system at higher energies.

### B. Non-extensivity parameter

The non-extensivity parameter, $q$, plays a significant role in the Tsallis statistics; it has been drawn as a function of $\eta$ at $\sqrt{s}$ = 0.9 and 2.36 TeV in Fig. 2(b). The figure shows that the value of $q$ increases with increasing $\eta$, which suggests the particles are emitted at higher $\eta$ away from the thermal equilibration. The calculated values of $r_{xy}$ for this plot are $+0.955 \pm 0.094$ for $\sqrt{s}$ = 0.9 TeV and $+0.990 \pm 0.045$ for $\sqrt{s}$ = 2.36 TeV, which points towards the strong positive correlation of the two parameters under consideration. In addition, one can see an inverse relationship between $q$ and $\sqrt{s}$, which suggests the system created at higher collision energy to be closer to thermal equilibrium at the same value of $\eta$.

### C. Volume of the produced system

Figure 2(c) displays $V$ versus $\eta$, with zero value of Pearson correlation coefficient for both $\sqrt{s}$ = 0.9 TeV and $\sqrt{s}$ = 2.36 TeV. The zero values of $r_{xy}$ show that $V$ is invariant under varying $\eta$. However, $V$ directly varies with $\sqrt{s}$ because of the greater pressure gradient in the higher-energy collisions, which results in the larger volume of the produced system.

### D. Mean transverse momentum

Mean transverse momentum, $\langle p_T \rangle$, is obtained from the fit function given in Eq. (9). Figure 3(a) represents $\langle p_T \rangle$ as a function of $\eta$, where the former decreases with increasing the latter due to the smaller energy deposition at higher $\eta$. For this plot, the values of $r_{xy}$ are calculated

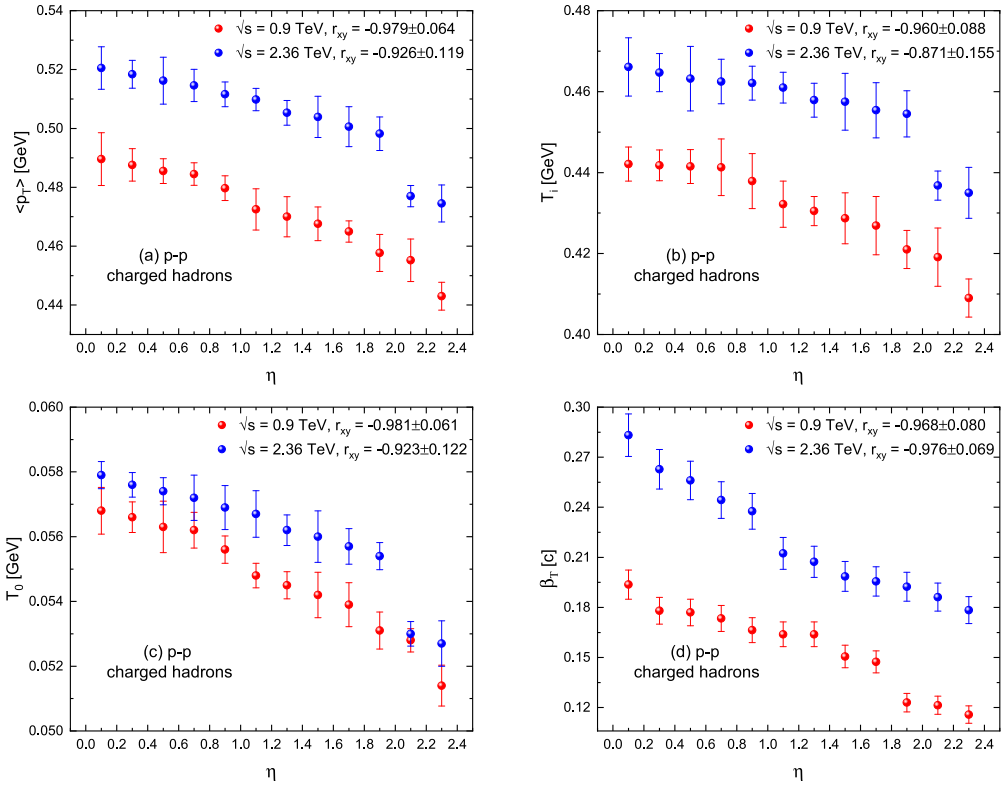


**Fig. 3.** (color online) (a) $\langle p_T \rangle$, (b) $T_i$, (c) $T_0$, and (d) $\beta_T$ calculated through the Eqs. (9), (12), (13), and (14), respectively for charged hadrons, as a function of $\eta$ in $p$-$p$ collisions at $\sqrt{s}$ = 0.9 TeV and 2.36 TeV. The Pearson correlation coefficients, $r_{xy}$, along with their errors are given in each plot.

to be $-0.979 \pm 0.064$ and $-0.926 \pm 0.119$ at $\sqrt{s}$ = 0.9 TeV and 2.36 TeV, respectively, which suggest a strong negative dependence of $\langle p_T \rangle$ on $\eta$. Figure 3(a) also indicates a direct relationship between $\langle p_T \rangle$ and $\sqrt{s}$.

### E. Initial temperature of the emission sources

Unlike the other temperatures such as chemical freeze-out temperature ($T_{ch}$), $T$, and $T_0$, which are associated with the later stages of the system's evolution, $T_i$ is linked with the initial stages of the collision, where the formation of the system is just taking place. This temperature can be calculated using the string Percolation model given in Eq. (12). Figure 3(b) shows $T_i$ as a function of the changing $\eta$ in $p$-$p$ collision at $\sqrt{s}$ = 0.9 TeV and 2.36 TeV. The values of $r_{xy}$ have also been calculated for this correlation along with their errors: $-0.960 \pm 0.088$ for 0.9 TeV and $-0.871 \pm 0.155$ for 2.36 TeV. The values of $r_{xy}$ indicate a strong negative dependence of $T_i$ on $\eta$. The system produced near the beam direction (along high $\eta$ regions) interacts with beams' remnants, due to which, it loses some of its energy, and as a result, the initial temperature along the beam direction falls. Meanwhile, along the mid rapidity, the colliding beams' remnants are almost absent and there is nothing to interact with in the initial stages of the created system, which leads to the higher initial temperature of the produced system. Moreover, Fig. 3(b) also shows the increasing behaviour of $T_i$ with increasing collision energies due to the violent collisions at higher energies.

### F. Kinetic freeze-out temperature

The Tsallis temperature, $T$, includes thermal and flow effects in the form of $T_0$ and $\beta_T$, respectively. For disentangling $T_0$ and $\beta_T$ from $T$, we used an alternative way given in Eq. (13) to calculate $T_0$. Figure 3(c) represents $T_0$ versus $\eta$, where the former decreases with increasing the latter due to the smaller energy deposition at higher $\eta$. For this plot, the values of $r_{xy}$ are calculated to be $-0.981 \pm 0.061$ and $-0.923 \pm 0.122$ at $\sqrt{s}$ = 0.9 TeV and 2.36 TeV, respectively, which indicate a strong negative dependence of $T_0$ on $\eta$. Figure 3(c) also shows a direct relationship between $T_0$ and $\sqrt{s}$.

$T_i$ is the temperature of the produced system at the early or initial stages just after the collision, $T$ is the effective temperature, which is related to the kinetic freeze-out stage and is the sum of the thermal and flow effects (already discussed in Section 2), and $T_0$ is the kinetic freeze-out temperature, which is the real temperature at the kinetic freeze-out stage. As the initial stage comes first and kinetic freeze-out stage follows, where substantial expansion and cooling have happened to the system and also $T$ is larger than $T_0$, the inequality $T_i > T > T_0$ oc-

curs.

### G. Transverse flow velocity

$\beta_T$ has been calculated using Eq. (14). Figure 3(d) represents the variation of $\beta_T$ with changing $\eta$. It can be seen that with decreasing $\eta$, $\beta_T$ increases because of the greater energy deposition in the mid rapidity region, which results in the greater pressure gradient in the low $\eta$ regions, causing the system to expand rapidly. $r_{xy} = -0.968 \pm 0.080$ and $-0.976 \pm 0.069$ at $\sqrt{s}$ = 0.9 TeV and 2.36 TeV, respectively, are the calculated values for the relationship between $\beta_T$ and $\eta$, suggesting a strong negative dependence of the former on the latter. Figure 3(d) also makes clear the direct variation of $\beta_T$ with $\sqrt{s}$ because at higher values of the latter, the squeeze in the produced system is maximum. As a result, a larger pressure gradient is produced, which leads to the rapid expansion of the fireball.

### H. Energy density

Energy density, $\varepsilon$, in the units of GeV/fm$^3$ has been obtained using Eq. (22) and is plotted against $\eta$ in Fig. 4(a). The figure shows that $\varepsilon$ is maximum at low $\eta$ and decreases as one moves towards the regions of high $\eta$. The reason for this dependence is that the energy transfer to the system, of almost constant volume at all values of $\eta$, is greater along the low values of $\eta$, which results in the higher energy density of the produced system. The values of $r_{xy}$ for this relationship are $-0.920 \pm 0.0124$ and $-0.937 \pm 0.110$ for $\sqrt{s}$ = 0.9 and 2.36 TeV, respectively, which suggest the strong negative dependence of $\varepsilon$ on $\eta$. In addition, this figure also indicates that $\varepsilon$ increases with increasing collision energy for the same reason as described for the dependence of $\varepsilon$ on $\eta$. Apart from this, Fig. 4(a) also displays a large gap between the values of $\varepsilon$ at the two colliding energies from $\eta = 0$ to approximately 1.3, and beyond this, towards the beam axis, they come close to each other. This shows the strong dependence of $\varepsilon$ on the collision energies at low $\eta$ compared to higher $\eta$.

### I. Particle density

Particle density, $n$, is calculated using Eq. (23) and is plotted against $\eta$ in Fig. 4(b). The figure displays an inverse dependence of the former on the latter. The reason for this negative dependence is that the energy availability for the new particle production at the lower $\eta$ is greater compared to higher $\eta$, at almost constant $V$ at all values of $\eta$, and hence results in the greater $n$ at lower $\eta$. $-0.926 \pm 0.119$ and $-0.897 \pm 0.140$ for $\sqrt{s}$ = 0.9 and 2.36 TeV, respectively, are the calculated values of $r_{xy}$ for this relationship, which indicate a strong negative correlation between the $n$ and $\eta$. This figure also shows increasing $n$ with increasing $\sqrt{s}$ because of the greater energy availability for the new particle production at higher collision energies. Figure 4(b) illustrates a substantial difference in the $n$ values between the two collision energies across the range of $\eta$ from 0 up to approximately 1.1. However, as the values extend beyond this range towards the beam axis, they converge closer to each other. This indicates that $n$ exhibits a more pronounced variation with collision energies at lower $\eta$ values compared to higher $\eta$.

### G. Entropy density

Entropy density, $s$, in the units of fm$^{-3}$ has been calculated using Eq. (24) and is represented as a function of $\eta$ in Fig. 4(c). The figure shows increasing $s$ with decreasing $\eta$. The greater energy deposition in the regions away from the beam direction, *i.e.*, at lower values of $\eta$, stimulates the greater disorder in the system of almost the same $V$ at different values of $\eta$, which eventually results in the greater entropy density. A strong negative dependence of $s$ on $\eta$ is also obvious from $r_{xy} = -0.959 \pm 0.090$ and $-0.935 \pm 0.112$ for $\sqrt{s}$ = 0.9 and 2.36 TeV, respectively. Similarly, for the same reasons, $s$ increases with increasing $\sqrt{s}$; this effect is obvious from the same figure. Figure 4(c) shows a notable distinction in the $s$ values between the two collision energies within the $\eta$ range of 0 to approximately 1.1. Nevertheless, as these values progress beyond this range towards the beam axis, they draw nearer to each other. This suggests that $s$ demonstrates a more significant change concerning collision energies at lower $\eta$ values compared to higher $\eta$ values.

### K. Pressure

Pressure, $P$, in the units of GeV/fm$^3$ has been obtained using Eq. (25) and is displayed as a function of $\eta$ in Fig. 4(d). The inverse dependence of $P$ on $\eta$ can be seen from the figure. A possible reason for this dependence is the greater pressure gradient in the system at the smaller values of $\eta$, as discussed earlier. The value of $r_{xy}$ for this relation for $\sqrt{s}$ = 0.9 TeV is $-0.906 \pm 0.134$ and for $\sqrt{s}$ = 2.36 TeV is $-0.926 \pm 0.119$, which show a strong negative relationship between these parameters. Figure 4(d) also displays the increasing behaviour of $P$ with increasing $\sqrt{s}$. Figure 4(d) illustrates a clear difference in the $P$ values between the two collision energies within the $\eta$ range from 0 to approximately 1.3. However, as these values extend beyond this range towards the beam axis, they tend to converge closer to each other. This indicates that $P$ exhibits a more pronounced variation in response to collision energies at lower $\eta$ values compared to higher $\eta$ values.

### L. Squared speed of sound

A parameter named squared speed of sound, $C_s^2$, has also been calculated using Eq. (27) for different $\eta$ intervals. The varying $C_s^2$ as a function of $\eta$ is displayed in Fig. 4(e). From this figure, one can deduce an inverse dependence of $C_s^2$ on $\eta$. This dependence suggests the pro-

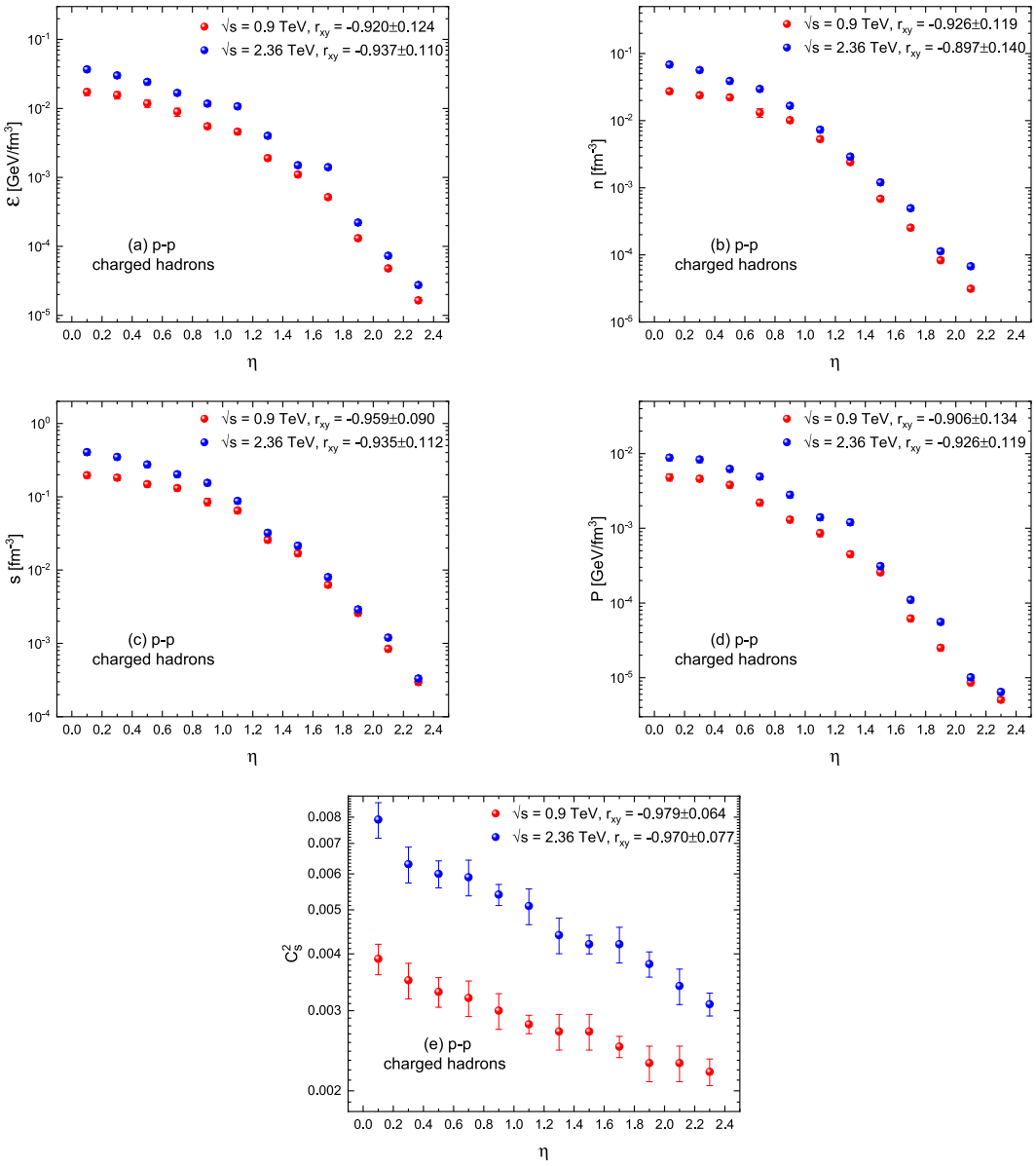


**Fig. 4.** (color online) (a) $\varepsilon$, (b) $n$, (c) $s$, (d) $P$, and $C_s^2$ calculated using Eqs. (22), (23), (24), (25), and (27), respectively, for charged hadrons versus $\eta$ at $\sqrt{s}$ = 0.9 TeV and 2.36 TeV in $p$-$p$ collisions. The Pearson correlation coefficients and their errors are also displayed in each plot. In this figure, the Y-axes of all plots are on a log scale.

duction of a stiffer medium or system along the low-$\eta$ regions compared to the regions with higher values of rapidity. The values of $r_{xy}$, which are $-0.979 \pm 0.064$ for $\sqrt{s} = 0.9$ TeV and $-0.847 \pm 0.030$ for $\sqrt{s} = 2.36$ TeV, represent a strong negative relationship between $C_s^2$ and $\eta$. In addition, this figure also reveals greater $C_s^2$ at $\sqrt{s}$ = 2.36 TeV than $\sqrt{s}$ = 0.9 TeV which again points towards the production of a stiffer medium at higher collision energy. Unlike $\varepsilon$, $n$, $s$, and $P$, the consistency in the fluctuation of $C_s^2$ remains constant across the entire $\eta$ range for both collision energies, as depicted in Fig. 4(e). This indicates an equal degree of sensitivity in $C_s^2$ at different collision energies, irrespective of the $\eta$ range.

Generally, the system produced in the p-p collision has a smaller density and temperature, due to smaller energy transfer in the collision, compared to the system produced in the nucleus-nucleus ($A$-$A$) collision. This leads to the production of a less stiff medium in $p$-$p$ collisions, which results in low $C_s^2$. The same explanation may apply to all other extracted and calculated parameters.

## IV. CONCLUSION

The Tsallis distribution was employed to analyse the transverse momentum distributions of charged hadrons generated in proton-proton collisions at energy levels of

$\sqrt{s}$ = 0.9 TeV and 2.36 TeV across various pseudorapidity classes. This analysis involved extracting key parameters, such as the effective temperature, non-extensivity parameter, and kinetic freezeout volume. We then computed the kinetic freezeout temperature and transverse flow velocity by an alternative method from the effective temperature. We further extracted the mean transverse momentum from the fit function and the initial temperature of the emission of source particles by the string percolation method. Similarly, using the effective temperature and non-extensive parameter, we calculated various thermodynamic quantities at the freeze-out stage, including energy density, particle density, entropy density, pressure, and squared speed of sound.

Besides the kinetic freezeout volume and non-extensivity parameter, other parameters demonstrate an increase as pseudorapidity decreases. This behavior can be linked to the greater energy transfer occurring along the mid-pseudorapidity region. The non-extensivity parameter rises with higher values of pseudorapidity, indicating that particles near the beam axis are far away from equilibrium. Interestingly, the kinetic freezeout volume appears to remain largely unaffected by changes in pseudorapidity. Moreover, the behavior of these parameters with collision energy shows a direct correlation, except for the non-extensivity parameter, which exhibits an inverse correlation. The values of $\varepsilon$, $n$, $s$, and $P$ at $\sqrt{s}$ = 0.9 TeV exhibit a considerable deviation from their corresponding values at $\sqrt{s}$ = 2.36 TeV within the $\eta$ range of 0 to approximately 1.2. However, as these values extend beyond this range towards the beam axis, they converge. This underlines a notable dependency of these parameters on collision energies, particularly pronounced at lower $\eta$ compared to higher $\eta$. Meanwhile, the consistency in the fluctuation of $C_s^2$ persists consistently throughout the entire $\eta$ range for both collision energies, indicating an equivalent sensitivity of $C_s^2$ across different collision energies, regardless of the $\eta$ range.

This study explicitly verifies the thermodynamic inequality $\varepsilon \geqslant 3P$, which is believed to exist only for such systems having extremely high densities compared to their internal pressure and hence suggests the formation of a QGP droplet. The analysis also confirms the inequality $T_i > T > T_0$, consistent with the evolution pattern of the generated fireball.

**Compliance with Ethical Standards** The authors declare that they are in compliance with ethical standards regarding the content of this paper.

## ACKNOWLEDGMENTS

*The authors are thankful to the Deanship of Graduate Studies and Scientific Research at University of Bisha for supporting this work through the Fast-Track research Support Program.*

## References


[1] S. A. Bass, M. Gyulassy, H. Stoecker *et al*., Journal of Physics G: Nuclear and Particle Physics **25**, R1 (1999)
[2] T. Matsui and H. Satz, Phys. Lett. B **178**, 416 (1986)
[3] P. Braun-Munzinger and J. Stachel, Nature **448**, 302 (2007)
[4] F. M. Liu and S. X. Liu, Phys. Rev. C **89**, 034906 (2014)
[5] A. Bialas and R. C. Hwa, Phys. Lett. B **253**, 436 (1991)
[6] I Arsene, I. G. Bearden, D. Beavis *et al*., Nucl. Phys. A **757**, 1 (2005)
[7] U. Heinz and M. Jacob, arXiv: nucl-th/0002042
[8] P. Podlaski, *Results on system size dependence of strangeness production in the CERN SPS energy range from NA61/SHINE*, in EPJ Web of Conferences (EDP Sciences) Vol. 276, p.03008
[9] M. J. Tannenbaum, Reports on Progress in Physics **69**, 2005 (2006)
[10] M. I. Abdulhamid, B. E. Aboona, J. Adam *et al*., Phys. Lett. B **845**, 138165 (2023)
[11] K. Aamodt, B. Abelev, A. Abrahantes Quintana *et al*., Phys. Rev. Lett. **105**, 252301 (2010)
[12] K. Aamodt, B. Abelev, A. Abrahantes Quintana *et al*., Phys. Rev. Lett. **107**, 032301 (2011)
[13] M. Gyulassy, *The QGP discovered at RHIC*, in *Structure and dynamics of elementary matter* (Netherlands, Springer, 2004), p. 159
[14] C. A. Bertulani and M. S. Hussein, Brazilian Journal of Physics **45**, 730 (2015)
[15] N. Herrmann, J. P. Wessels, and T. Wienold, Annual Review of Nuclear and Particle Science **49**, 581 (1999)
[16] U. Heinz and R. Snellings, Annual Review of Nuclear and Particle Science **63**, 123 (2013)
[17] P. Bozek, arXiv: 0911.2392v2 [nucl-th]
[18] T. Kalaydzhyan and E. Shuryak, Phys. Rev. C **91**, 054913 (2015)
[19] J. Adam *et al*. (ALICE Collaburation), Nature Phys. **13**, 535 (2017)
[20] R. Sahoo and T. K. Nayak, Current Science **121**, 1403 (2021)
[21] R. Sahoo, AAPPS Bulletin **29**, 16 (2019)
[22] S. Acharya *et al*. (ALICE Collaboration), Eur. Phys. J. C **80**, 693 (2020)
[23] V. Khachatryan, A. M. Sirunyan, A. Tumasyan *et al*., Phys. Rev. Lett. **116**, 172302 (2016)
[24] S. Jena and R. Gupta, Phys. Lett. B **807**, 135551 (2020)
[25] O. Ristea, C. Ristea, and A. Jipa, International Journal of Modern Physics E **31**, 2250090 (2022)
[26] A. S. Parvan and T. Bhattacharyya, Eur. Phys. J. A **56**, 72 (2020)
[27] A. S. Parvan, Journal of Physics G: Nuclear and Particle Physics **50**, 125002 (2023)
[28] S. Tripathy, T. Bhattacharyya, P. Garg *et al*., Eur. Phys. J. A **52**, 289 (2016)
[29] M. Badshah, M. Waqas, A. M. Khubrani *et al*., Europhys.

Lett. **141**, 64002 (2023)
[30] M. Badshah, M. Ajaz, M. Waqas *et al*., Physica Scripta **98**, 115306 (2023)
[31] M. Waqas, G. X. Peng, and F. H. Liu, Journal of Physics G: Nuclear and Particle Physics **48**, 075108 (2021)
[32] M. Badshah, A. Haj Ismail, M. Waqas *et al*., Symmetry **15**, 1554 (2023)
[33] J. Cleymans and D. Worku, Journal of Physics G: Nuclear and Particle Physics **39**, 025006 (2012)
[34] H. L. Lao, F. H. Liu, B. C. Li *et al*., Nuclear Science and Techniques **29**, 82 (2018)
[35] H. R. Wei, F. H. Liu, and R. A. Lacey, Journal of Physics G: Nuclear and Particle Physics **43**, 125102 (2016)
[36] M. Badshah, M. Waqas, M. Ajaz *et al*., Journal of Physics G: Nuclear and Particle Physics **51**, 065109 (2024)
[37] W. H. Wu, J. Q. Tao, H. Zheng *et al*., Nuclear Science and Techniques **34**, 151 (2023)
[38] P. P. Yang, F. H. Liu, and K. K. Olimov, Entropy **25**, 1571 (2023)
[39] L. J. Gutay, A. S. Hirsch, C. Pajares *et al*., International Journal of Modern Physics E **24**, 1550101 (2015)
[40] R. P. Scharenberg, B. K. Srivastava, and C. Pajares, Phys. Rev. D **100**, 114040 (2019)
[41] P. Sahoo, S. De, S. K. Tiwari *et al*., Eur. Phys. J. A **54**, 1 (2018)
[42] L. L. Li, F. H. Liu, M. Waqas *et al*., Advances in High Energy Physics **2020**, 1 (2020)
[43] I. U. Bashir and S. Uddin, Communications in Theoretical Physics **68**, 500 (2017)
[44] V. Khachatryan *et al*. (CMS collaboration), JHEP **2010**, 41 (2010)
[45] K. K. Olimov, I. A. Lebedev, A. I. Fedosimova *et al*., Eur. Phys. J. Plus **138**, 1 (2023)